

Integrated AFM and SECM for in situ studies of localized corrosion of Al alloys

A. Davoodi^a, J. Pan^{a,*}, C. Leygraf^a, S. Norgren^b

^a Division of Corrosion Science, Department of Materials Science and Engineering,
Royal Institute of Technology, SE-100 44 Stockholm, Sweden

^b Sapa Heat Transfer AB, SE-61281 Finspång, Sweden

Received 18 July 2006; received in revised form 17 November 2006; accepted 17 December 2006

Available online 25 January 2007

Abstract

Rolled 3xxx series Al alloys, e.g., EN AW-3003, are generally used as fin or tube material in heat exchangers for automobiles. With reducing fin thickness, maintaining fin material integrity is of increasing importance. This study aimed at exploring the differences in intrinsic corrosion properties between EN AW-3003 and a newly developed Al–Mn–Si–Zr fin alloy using state-of-the-art local probing techniques. Volta potential mapping of both alloys by scanning Kelvin probe force microscopy (SKPFM) indicates a cathodic behaviour of constituent intermetallic particles ($>0.5\ \mu\text{m}$) relative to the alloy matrix. Compared to EN AW-3003, the Al–Mn–Si–Zr alloy has a smaller number of particles with large Volta potential difference relative to the matrix. In situ atomic force microscopy (AFM) measurements in slightly corrosive solutions showed extensive localized dissolution and deposition of corrosion products on EN AW-3003, and only a small number of corroding sites and “tunnel-like” pits on Al–Mn–Si–Zr. Probing the ongoing localized corrosion process by integrated AFM and scanning electrochemical microscopy (SECM) revealed more extensive local electrochemical activity on EN AW-3003 than on Al–Mn–Si–Zr. In all, the lower corrosion activity and smaller tunnel-like pits resulted in lower material loss of the Al–Mn–Si–Zr alloy, a beneficial property when striving towards thinner fin material.

© 2007 Elsevier Ltd. All rights reserved.

Keywords: Al alloy; Localized corrosion; SKPFM; In situ AFM; Integrated in situ AFM/SECM

1. Introduction

Heat exchangers with tube and fin components, such as radiators in automobiles, are today mainly produced using Al alloys. Tubes and fins are brazed together using a brazing Al–Si alloy having a lower eutectic temperature than the tube or fin core alloy. For the past 15 years, the standard commercial Al alloy for heat exchanger applications is the EN AW-3003 (AA3003) Al alloy containing about 1 wt.% Mn, having good formability, mechanical strength and acceptable corrosion performance. The alloy developments using basic EN AW-3003 composition have improved the corrosion resistance, especially of tube alloys, so called “long-life” alloys. For alloys used as fins, the long-term mechanical and corrosion performance is of increasing importance as down-gauging of strip continues, to 70 μm thickness

or even less. When required, i.e., during exposure to corrosive environment, the fin material should act as an efficient sacrificial anode to protect the tube from being perforated. In addition, it should have a high intrinsic corrosion resistance to maintain material integrity and mechanical properties in a long service. Developing new fin alloys with improved intrinsic corrosion properties requires a detailed understanding of the corrosion mechanisms of these alloys.

Different localized corrosion mechanisms have been observed on Al alloys in different solutions [1–4]. For pure Al with crystallized structure, pitting develops along closely packed (100) planes resulting in crystallographic corrosion [1–3]. Alloying generally leads to the initiation and development of pits that are less sensitive to the microstructure of the alloy matrix, but more related to the secondary phases. Corrosion of low-alloyed Al alloys is slightly localized along grain boundaries. A further increase in the content of alloying elements enhances the localization of pitting, because the amount of intermetallic phases increases substantially. High-alloyed Al alloys are often

* Corresponding author. Tel.: +46 8 790 6739; fax: +46 8 208284.
E-mail address: jinshanp@kth.se (J. Pan).

Table 1
Chemical composition (wt.%) of the Al alloys investigated

Material	Gauge (mm)	Si	Fe	Cu	Mn	Mg	Zn	Zr
EN AW-3003	0.10	0.15	0.48	0.12	1.1	0.03	<0.01	–
Al–Mn–Si–Zr	0.10	0.73	0.24	0.04	1.6	0.01	0.03	0.11

susceptible to intergranular corrosion. One of the reasons is that the structure of the grain boundaries becomes more complicated due to the appearance of precipitates, zones depleted of alloying elements, and zones enriched in certain alloying elements and dislocation piles [3–5]. A tunnel-like pitting and narrow long channels have been observed on some commercial Al alloys, depending on microstructure, solution composition, electrode potential and temperature [1–3]. The reason for this type of behavior was discussed in terms of coupling of dissolution and mass transport [6]. Some studies suggest that the alkalinity developed at cathodic intermetallic particles on Al alloys in aerated solutions can dissolve the adjacent alloy matrix, creating grooves or pit-like clusters [7–10]. Later these cavities may switch to an acid-pitting mechanism [7]. Other authors, however, refer to the alkaline attack as pitting or treat the problem as galvanic corrosion between particle and matrix [9], or self-regulating cathodic reaction occurring on the particles [10].

During the last decade, local probing techniques such as atomic force microscopy (AFM) [7], scanning Kelvin probe force microscopy (SKPFM) [11–13], and scanning electrochemical microscopy (SECM) [14,15] have been used for investigation of local corrosion mechanisms of Al alloys. However, such studies of 3xxx series Al alloys are scarce in the literature. Recently, an integrated AFM and SECM system with micro- or submicron resolution has been applied for in situ study of localized corrosion of Al alloys [16,17]. Concurrent AFM topography and SECM electrochemical activity mapping provided detailed information of ongoing localized corrosion process of Al alloys related to the intermetallic particles.

This paper reports a comparative study of localized corrosion of a standard EN AW-3003 alloy and a new fin alloy (Al–Mn–Si–Zr) developed at Sapa Heat Transfer AB. Scanning electron microscopy (SEM) with energy dispersive X-ray spectroscopy (EDS) was used for characterisation of the microstructure and particle composition. SKPFM was applied to map Volta potential of intermetallic particles relative to the alloy matrix. In addition to more conventional corrosion tests and electrochemical polarization measurements, in situ AFM and integrated AFM/SECM were used in situ to investigate the influence of material heterogeneities on localized corrosion properties of the two Al alloys.

2. Experimental

2.1. Sample material and preparation

The two 3xxx (Al–Mn) series materials investigated are a standard EN AW-3003 alloy, and a new fin alloy denoted Al–Mn–Si–Zr alloy, which has a very low Cu content, an

increased Si and Mn content and some addition of Zr. Their chemical compositions (wt.%) are given in Table 1. The materials were DC cast to 600 mm size ingots, scalped and hot rolled. The EN AW-3003 alloy was submitted to a homogenisation heat treatment prior to hot rolling, while this process was omitted for the Al–Mn–Si–Zr alloy. Normal practises for cold rolling, including an annealing step and a final reduction, were employed. To simulate a brazing process, sheets of the investigated materials were submitted to heating and cooling cycles following normal industrial procedures. Air was avoided either by using a vacuum furnace or filling the furnace with nitrogen. For traditional electrochemical measurements, the as-received surface was cleaned by ethanol prior to the experiments. For microstructure characterization and local electrochemical measurements, small samples (0.5 mm × 0.1 mm) were cut and embedded in epoxy. Each surface investigated was sectioned longitudinally to the rolling direction, ground and polished following normal procedures at Sapa Technology AB, with a final polishing step using a colloidal silica suspension about pH 10, and subsequently cleaned in ethanol.

2.2. Solutions and electrochemical cell

Accelerated corrosion testing of strip samples of 60 mm × 110 mm size was performed according to the standard practice for modified salt spray (fog) testing established as the SWAAT test. The SWAAT corrosion test followed the ASTM G85-02, Annex A3 using a test solution containing 42 g/L synthetic sea salt without heavy metals, in accordance to ASTM D1141-98. The step of adjusting the pH to 8.2 prior to the glacial acetic acid addition was omitted. The final pH after addition of 10 mL/L glacial acetic acid was balanced to pH 2.85 using 1 M NaOH. The SWAAT test includes a 2 h cycle with 30 min intermittent salt spray, followed by a 90 min soak at above 98% relative humidity. The test cabinet temperature was controlled at 49 °C. This SWAAT solution was also used in the electrochemical AFM measurements where the pH was adjusted to 4 in order to avoid too fast dissolution. For the integrated AFM/SECM study, a diluted solution of 20 mM NaCl + 2 mM KI (pH 6.5) was used to investigate initial stage of the localized corrosion. KI was added as redox mediator for SECM mapping of electrochemical current in the solution. KI was chosen for convenience, and previous experiments showed that KI could be satisfactorily used for this purpose [16]. It is believed that the effect of I[−] ions as additional corrosive species is not of importance for this chloride solution. Reagent NaCl, KI and distilled water were used to make up the solution. A standard three-electrode cell for corrosion study was used for the traditional electrochemical measurements. For the local electrochemical study, a small electrochemical cell made of Teflon was used, with solution layer of ca. 1.5 mm in thickness

covering the sample surface. A saturated Ag/AgCl was used as the reference electrode, and a Pt foil surrounding the sample as the counter electrode.

2.3. Instruments and techniques

A standard SEM/EDS instrument was used for microstructure characterization and composition analysis of intermetallic particles. To evaluate the relative nobility of the intermetallic particles of the Al alloys, the Volta potential variations were mapped through SKPFM measurements, the principle and details of the technique have been described previously [11–13]. In this work, a commercial AFM instrument supplied by Veeco Thermomicroscopes was used, and the relative humidity in the chamber was 40% [18]. The probe was a heavily doped silicon tip with a nominal spring constant of 2 N/m, suitable for both the Volta potential mapping and for imaging the sample surface. The Volta potential was measured using a standard non-contact force detection technique, and the tip was held at a fixed distance of approximately 100 nm above the sample. Standard electrochemical polarization measurements were performed by using an EG&G 273A potentiostat.

For the in situ AFM and integrated AFM/SECM measurements, the instrument used was a Resolver from Quesant Ltd., equipped with the iProbe package supplied by Windsor Scientific Ltd., UK. Details of the AFM/SECM instrument have been described previously [16,17]. The in situ AFM was performed using a triangle contact mode cantilever (from Quesant Instrument Co.) made of an oxide sharpened silicon nitride, with nominal spring constant 0.12 N/m. The integrated AFM/SECM was performed using a dual mode cantilever/tip probe. The dual mode probe is a “L” shaped ultramicroelectrode, with a Pt wire insulated in a fiber glass (different from previously used probe). The arm is flattened for laser reflection. At the end of the bending part, the probe diameter is 10 μm and the Pt core diameter is ca. 1 μm . It has a 25° inclination so that the sharp end point acts as the AFM tip, and the inclination keeps a constant distance (ca. 2 μm in contact mode) between the sample and Pt ultramicroelectrode for the SECM mapping. In the integrated AFM/SECM measurement, the first line scan is a normal AFM operation in contact mode and a line of surface profile was collected. Then the

feedback is stopped and the tip is withdrawn to a preset distance (a few nm to a few μm) from the surface, and in the second line scan the tip follows the surface profile obtained from the first scan, and collects the local current using a redox couple as mediator. With a normal scan speed (2 Hz) it takes a few minutes to acquire a pair of AFM and SECM images. In the case of a very small lift (<10 nm), the system operates in one pass mode while acquiring two signals (topography and current) simultaneously.

The SECM was operating in sample-generator-tip-collector mode using I^-/I_3^- as the redox mediator. The voltammogram of the ultramicroelectrode tip in the solution containing the redox mediator was characterized by using the iProbe potentiostat to define the working potential range of the ultramicroelectrode. Examples of CV curves of the KI redox mediator on the ultramicroelectrode were reported previously [16]. By scanning over the surface, concurrent AFM topography and SECM current maps were obtained of the same area. During the measurement, the sample was held at open circuit potential or anodically polarized. Local surface areas of higher anodic activity result in reduction of the redox mediator at such areas, diffusion towards the tip and subsequent oxidation of the redox mediator at the tip. The lateral resolution of the SECM depends on the tip size, the sample-tip distance and the electrolyte conductivity [19].

3. Results and discussion

3.1. General corrosion behaviour

Fig. 1 shows the surface appearance after 4 days immersion in the SWAAT solution of the EN AW-3003 and Al–Mn–Si–Zr samples submitted to the simulated brazing heating cycle. The corrosion products were removed by washing after the corrosion test. It is clear that the EN AW-3003 alloy exhibits wide pits and extensive perforation and, hence, a large material loss. In comparison, on the Al–Mn–Si–Zr alloy the pits are small (tunnel-like) and perforation is limited, and therefore the impact on the material integrity is relatively small. The measured weight loss was about two times higher for the EN AW-3003 than the Al–Mn–Si–Zr. Note that this was an accelerated corrosion test, with exposure conditions far from normal operation. Hence, it is desirable to investigate corrosion processes under

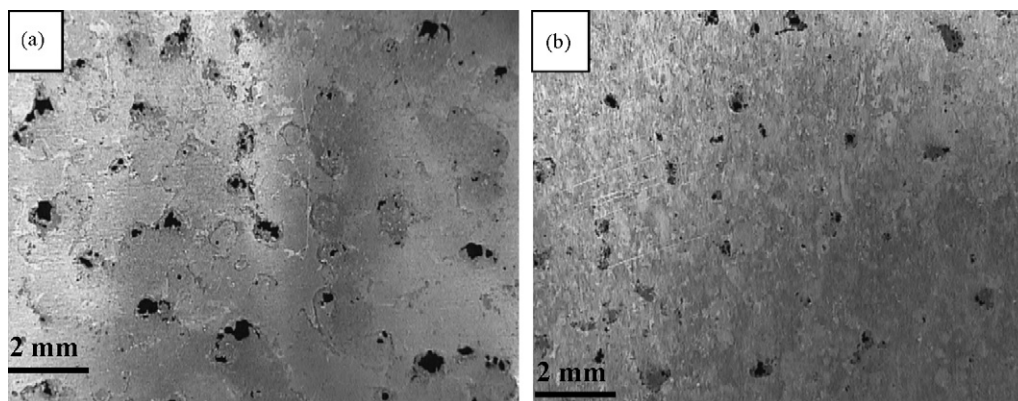


Fig. 1. Surface appearance after 4 days immersion in SWAAT solution: (a) EN AW-3003 and (b) Al–Mn–Si–Zr.

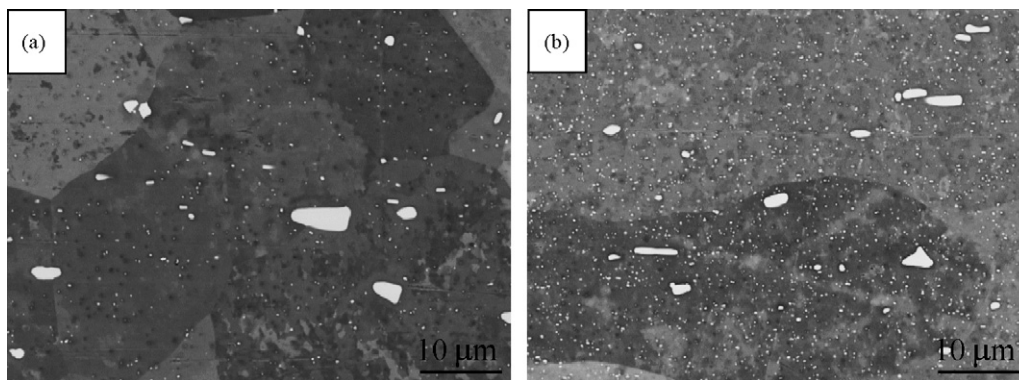


Fig. 2. Backscatter SEM images of polished (a) EN AW-3003 and (b) Al-Mn-Si-Zr. The intermetallic particles appear bright.

more realistic conditions, especially the initial stage of localized corrosion.

3.2. Characterization of intermetallic particles

Fig. 2 shows backscatter SEM images of sections in the longitudinal direction. Intermetallic particles appear brighter in the images due to their higher atomic number compared to the Al matrix. The larger particles (μm in size), named constituent particles, are seen in both alloys. There is also a larger amount of fine particles (white dots, $<0.5 \mu\text{m}$, often $50\text{--}200 \text{ nm}$), in what follows named dispersoids, present in the Al-Mn-Si-Zr alloy as compared to the standard EN AW-3003 alloy. EDS analysis of larger particles ($>2 \mu\text{m}$) showed that the EN AW-3003 alloy contains mainly particles of $\text{Al}_6(\text{Mn, Fe})$ type and some of the $\text{Al}_{12}(\text{Mn, Fe})_3\text{Si}$ type, in both cases with a Mn/Fe ratio of 1:1. There is basically only one type of larger particles in the Al-Mn-Si-Zr alloy, the $\text{Al}_{12}(\text{Mn, Fe})_3\text{Si}_2$ in which the Mn/Fe ratio is 4:1. The fine dispersoids normally have the composition of $\text{Al}_{12}\text{Mn}_3\text{Si}_{1-2}$. Determined by resistivity/thermoelectric power measurements, the concentration of Mn in solid solution is about 0.44 wt.% in the EN AW-3003, and 0.24 wt.% in the Al-Mn-Si-Zr alloy.

3.3. Volta potential mapping

Volta potential mapping of the polished sample surface of the two alloys were achieved by SKPFM measurements. From concurrent topography and Volta potential images obtained by this technique, the Volta potential variations can be clearly correlated to the intermetallic particles in the alloy matrix. Generally, the Volta potential is regarded as a measure of relative nobility of the material [11,13]. Since the absolute values are sensitive to many factors and require careful calibration of the measuring system, the discussion herein is focused only on the Volta potential difference between the particles and the alloy matrix, which is of interest when considering galvanic effects on localized corrosion processes.

As an example, Fig. 3 shows concurrent AFM topography and Volta potential images, and Fig. 4 displays Volta potential maps illustrating variations between the matrix and larger or smaller particles. Generally, the constituent particles ($>0.5 \mu\text{m}$)

in both alloys exhibit a higher Volta potential (brighter areas in the images) than the alloy matrix, which indicate their cathodic character relative to the matrix. Roughly the Volta potential difference relative to the matrix is around 300–600 mV for the larger particles ($2\text{--}6 \mu\text{m}$), and around 100–300 mV for the smaller particles ($0.5\text{--}2 \mu\text{m}$). The Al-Mn-Si-Zr alloy contains a smaller number of particles having a larger potential difference relative to the matrix. In some cases, it appears that the Volta potential has a minimum in a narrow boundary region between large particles and the matrix. Further measurements are needed to verify this observation. On the other hand, no clear difference in Volta potential between the fine dispersoids (ca. 50 nm) and the matrix can be seen, except some larger dispersoids having the size of a few hundreds of nanometers. Since the relation between Volta potential and local electrochemistry is relevant but not trivial, it is desirable to combine this information with local electrochemical data and corrosion morphology [13].

3.4. In situ AFM observation of localized corrosion

In situ AFM measurements were performed at open circuit potential for the two alloys after different times of exposure in the SWAAT solution adjusted to pH 4 (less aggressive). The AFM images obtained show in detail the progress of localized dissolution and formation of the corrosion products on the surface. The results reveal a certain difference in the localized corrosion behaviour between the two alloys. As an example, Fig. 5 shows in situ AFM images of EN AW-3003 and Al-Mn-Si-Zr alloys after 2 days in the solution. Clearly a large number of corroding sites are evident on the EN AW-3003 alloy, where precipitates of the corrosion products were formed on the surface. This indicates that extensive local dissolution has occurred on this alloy. In contrast, only a small number of corroding sites are observed on the Al-Mn-Si-Zr alloy, and the precipitates of corrosion products are relatively small. This indicates that the fine dispersoids (much more in the Al-Mn-Si-Zr alloy) are not active in localized corrosion processes. The corroding sites are most likely related to the cathodic intermetallic particles that have sufficiently high Volta potential difference relative to the matrix, so that local anodic dissolution of the matrix starts in the boundary region adjacent to the particles. The observation is in accordance with the Volta potential mapping, which revealed

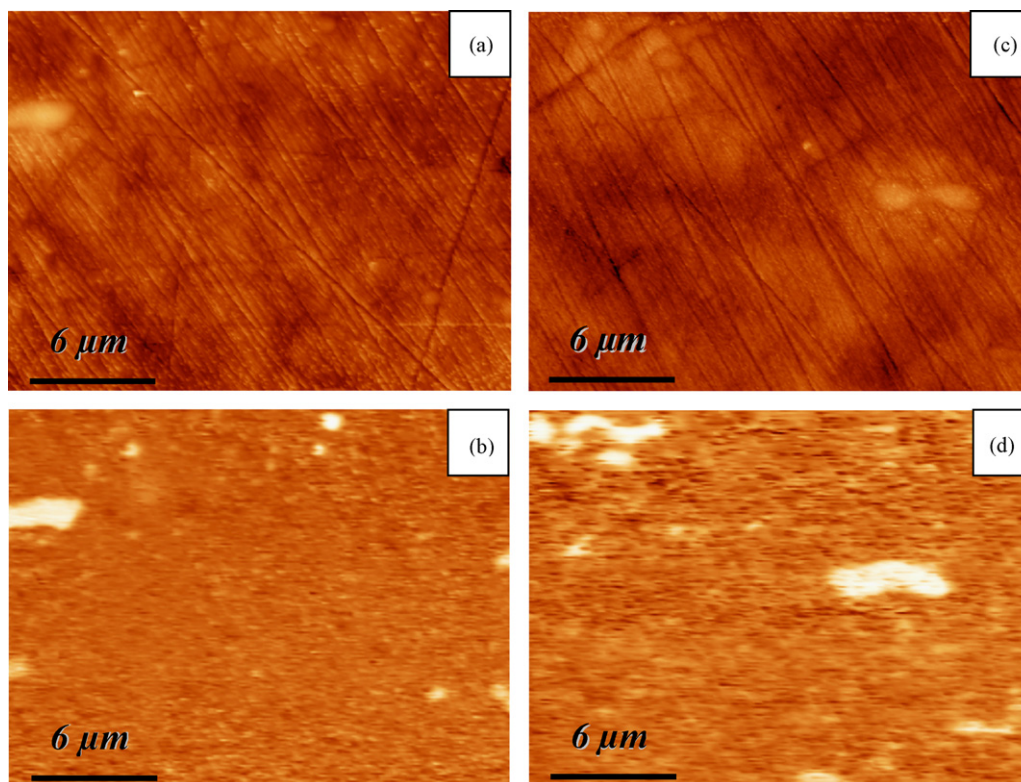


Fig. 3. AFM topography (a and c) and Volta potential map (b and d) of polished EN AW-3003 (left) and Al-Mn-Si-Zr (right), respectively. Higher Volta potential (brighter) of the intermetallic particles indicates a cathodic character compared to the matrix.

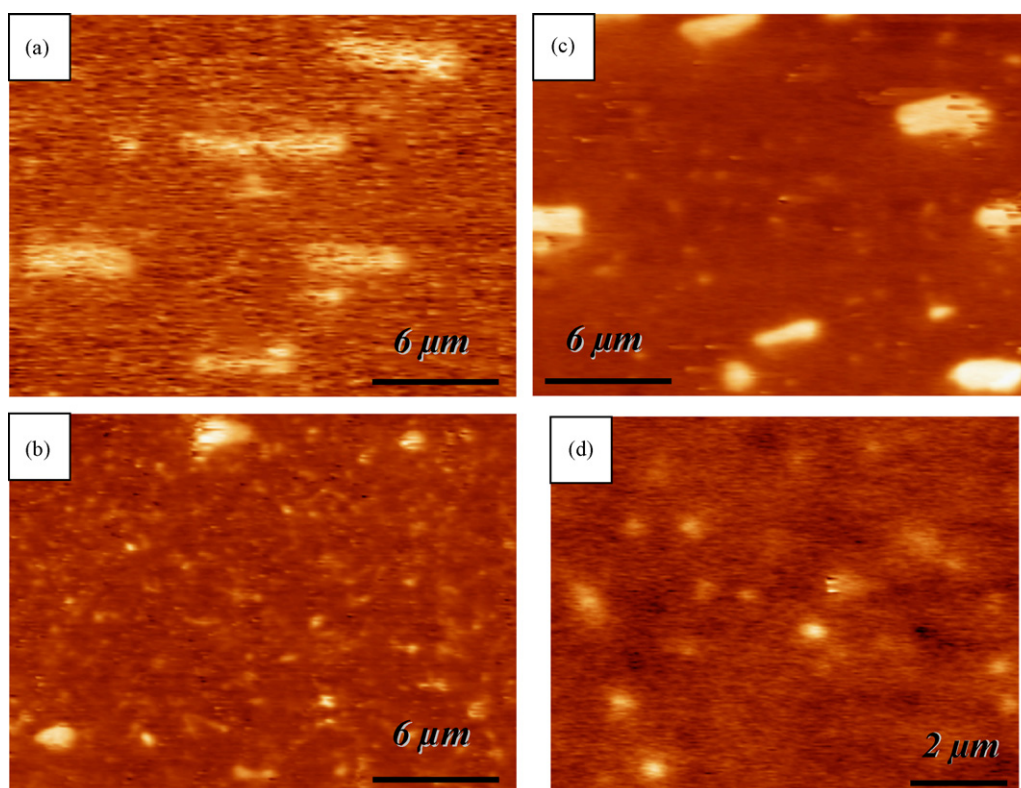


Fig. 4. Volta potential maps of polished (a and b) EN AW-3003 and (c and d) Al-Mn-Si-Zr, showing higher Volta potential (brighter) of larger micrometer sized particles (a and c) and smaller particles of a few hundreds nanometer in size (b and d).

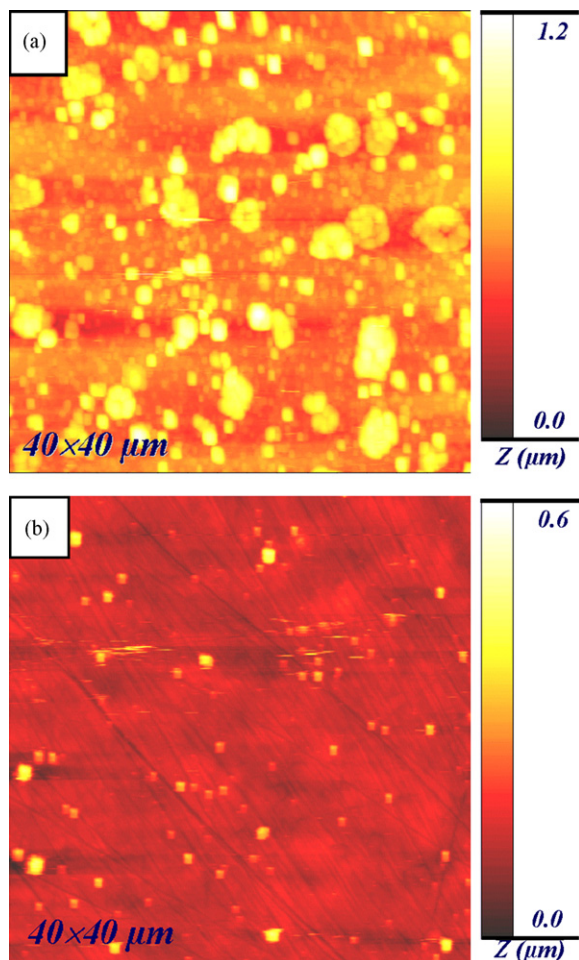


Fig. 5. In situ AFM images of (a) EN AW-3003 and (b) Al-Mn-Si-Zr, after 2 days in SWAAT solution of pH 4, showing precipitates of corrosion products, much less on the Al-Mn-Si-Zr alloy.

a smaller number of intermetallic particles having large Volta potential difference relative to the matrix on the Al-Mn-Si-Zr alloy as compared EN AW-3003.

The in situ AFM observation also shows a certain difference in microscopic corrosion mode between the two alloys. As an example, Fig. 6 displays in situ AFM images of a small area (several micrometer) of the EN AW-3003 and Al-Mn-Si-Zr alloy after 2 days in the solution. Ring-like deposits consisting of “rectangular bricks” were clustered around wide pits on EN AW-3003, whereas small pits in an early stage were formed on Al-Mn-Si-Zr with small deposits around the pits. Fig. 7 shows the in situ AFM images obtained after 3.5 days. In addition to extensive local dissolution and formation of precipitates of corrosion products, intergranular corrosion along grain boundaries also occurred on EN AW-3003. In contrast, pitting was the main feature on the Al-Mn-Si-Zr, and the pits still maintained their localized form despite of some growth in depth and size, characteristic of tunnel-like pitting. The precipitates of corrosion products are probably Al hydroxide, which is formed where Al ions become oversaturated due to local dissolution of the Al matrix. The highly localized corrosion, i.e., tunnel-like pitting, of the Al-Mn-Si-Zr alloy implies minor perforation and a low

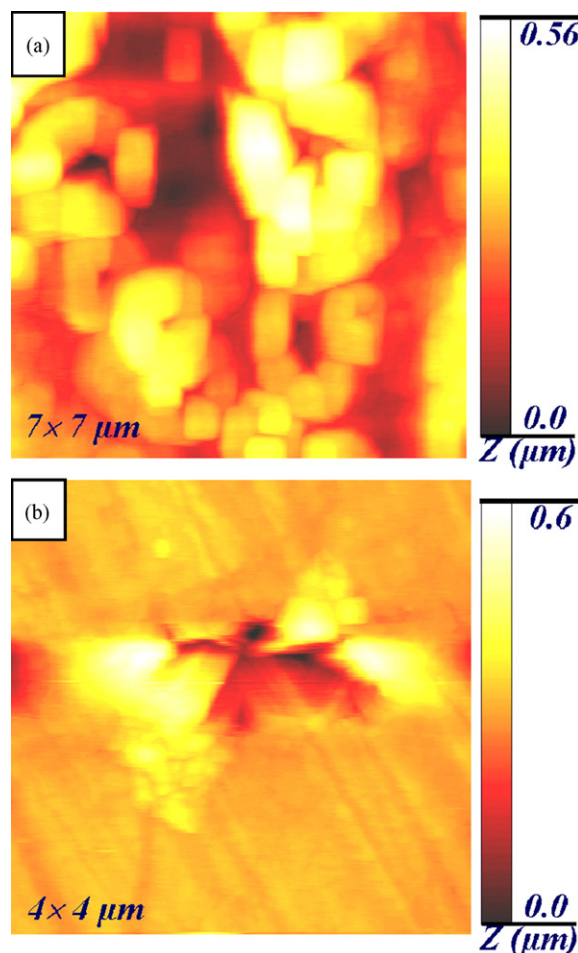


Fig. 6. In situ AFM images of (a) EN AW-3003 and (b) Al-Mn-Si-Zr, after 2 days in SWAAT solution of pH 4. Ring-like deposits clustered around wide pit on the EN AW-3003 alloy, whereas early stage of pit observed on the Al-Mn-Si-Zr alloy.

impact on the material integrity. Therefore, this alloy is favorable for fin applications, especially when thinner fin material is required.

3.5. Integrated AFM/SECM probing of pitting initiation

Before the integrated AFM/SECM investigation, normal cyclic potentiodynamic polarization measurements were performed to define the potential regions of interest for local electrochemical study. As an example, Fig. 8 shows the cyclic polarization curve of EN AW-3003 exposed to 10 mM NaCl solution in aerated condition. As can be seen, the open-circuit potential was ca. -0.71 V versus Ag/AgCl, a passive region was evident up to ca. -0.58 V versus Ag/AgCl, and above that potential breakdown of passivity occurred, leading to a drastically increased current density and the hysteresis loop upon reversed potential sweep. In this case, the potential region for AFM/SECM studies was chosen from the open circuit potential to 200 mV anodic polarization, in order to investigate pre-pitting events in the passive region and pitting initiation processes near and above the breakdown potential. Based on the voltammogram characterization of the SECM ultramicroelectrode in the work-

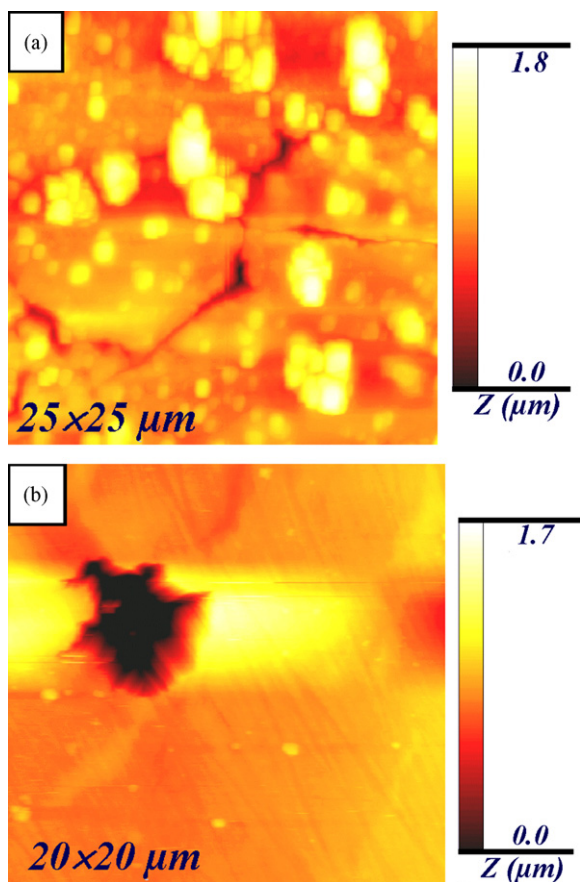


Fig. 7. In situ AFM images of (a) EN AW-3003 and (b) Al-Mn-Si-Zr, after 3.5 days in SWAAT solution of pH 4. Intergranular attack along grain boundaries observed on the EN AW-3003 alloy and tunnel-like pitting in the Al-Mn-Si-Zr alloy.

ing solution, the probe potential was controlled at ca. 600 mV versus Ag/AgCl for maximal collection of the local electrochemical current. Moreover, finite element method (FEM) simulation of the SECM in the integrated AFM/SECM configuration was performed, which indicates that micrometer lateral resolution of the SECM can be obtained by the instrument. The

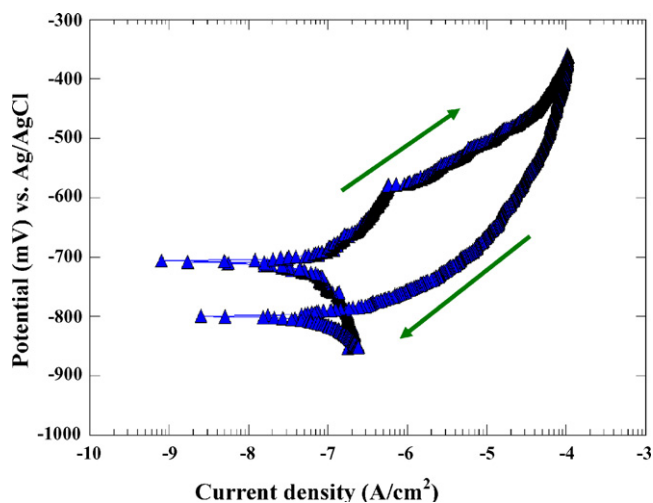


Fig. 8. Cyclic polarization curve of EN AW-3003 alloy in 10 mM NaCl solution.

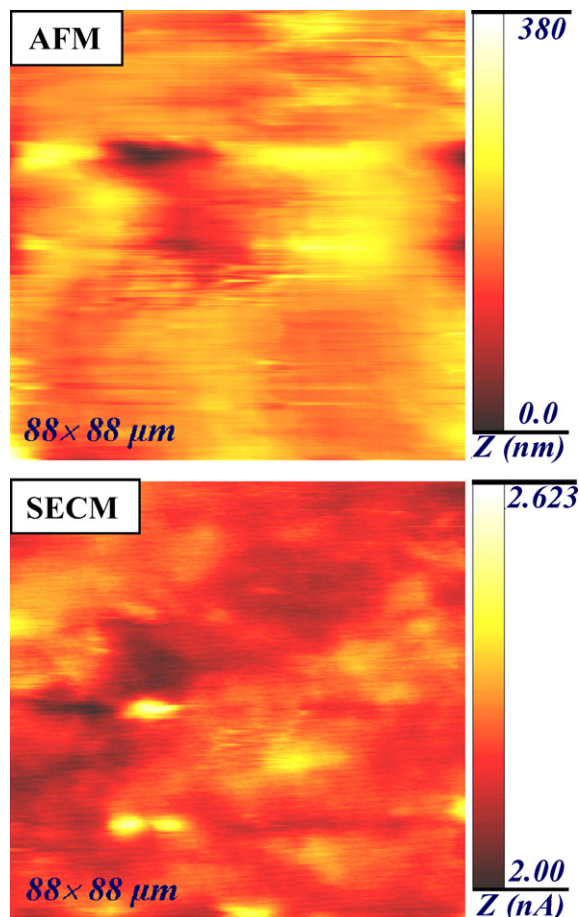


Fig. 9. Concurrent in situ AFM and SECM images of EN AW-3003 alloy in 20 mM NaCl + 2 mM KI solution during small polarization in the passive region. Pitting precursors are displayed.

lateral resolution of about 1 μm was verified in the AFM/SECM measurements of the Al alloys (to be published elsewhere).

The integrated AFM/SECM probing of the EN AW-3003 surface in 20 mM NaCl solution containing 2 mM KI as mediator revealed local anodic current and topography changes associated with precursors of pitting in the passive potential region, and also extensive local active dissolution above the breakdown potential. Fig. 9 shows concurrent AFM and SECM images of the EN AW-3003 at about 100 mV anodic polarization (passive potential region). Generally, the quality of the topography images obtained by the dual mode probe is lower than what can be achieved by a standard AFM cantilever, like in the EC-AFM results above. The reason is that the dual mode probe utilizes the end point of the fiber glass (quartz) as AFM tip in compromise for the ultramicroelectrode. Sometimes, a higher scan speed (ca. 4 Hz) is needed in order to catch fast ongoing electrochemical activities on the surface (e.g., passivity breakdown) by SECM, and this may lead to a lower vertical resolution of the AFM images, as exemplified in Fig. 9. This may be improved by optimisation of design of the dual mode probe in future.

As can be seen in Fig. 9, with such a small polarization, local anodic current (brighter areas in the SECM image) could be observed on the smooth surface (AFM image). Since the local current was stable for at least a couple of minutes, i.e., the dura-

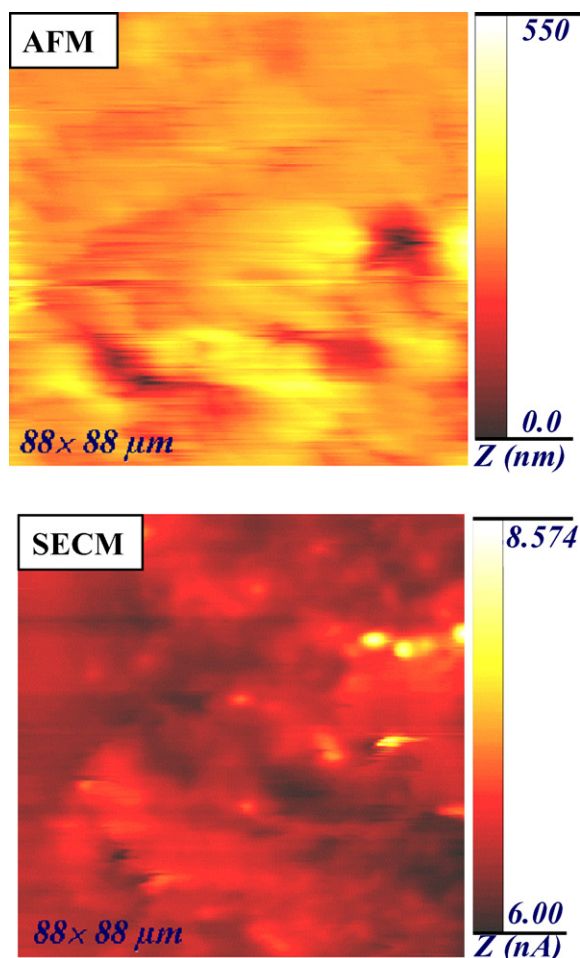


Fig. 10. Concurrent in situ AFM and SECM images of EN AW-3003 alloy in 20 mM NaCl + 2 mM KI solution during 200 mV anodic polarization. Progress in localized corrosion observed characterized by active areas of small extension.

tion of the AFM/SECM measurement, these sites are regarded as pitting precursors, probably related to local dissolution of the matrix adjacent to certain intermetallic particles. Fig. 10 shows concurrent AFM and SECM images of EN AW-3003 in the solution at 200 mV anodic polarization (above breakdown potential). A large number of active areas with enhanced anodic current could be observed in the SECM image while a pit-like hole appeared in the AFM image. The background current (z -scale) in the SECM image was significantly increased compared to the image obtained in the passive region. This is due to extensive localized anodic dissolution occurring on the surface. The sequence of the AFM/SECM images obtained by repeated measurements on the same area revealed that the current of local active areas varies with time while the pit grows. Fig. 11 displays the SECM image in three dimensions, showing clearly different current levels in different active areas. It was also observed that, even when the anodic polarization was reduced into the passive region, there are still areas of enhanced local current despite of a reduced background current level, and the pits continue to grow slightly. This remaining local anodic activity at reduced polarization after passivity breakdown can explain the hysteresis loop in the cyclic polarization curve in Fig. 8.

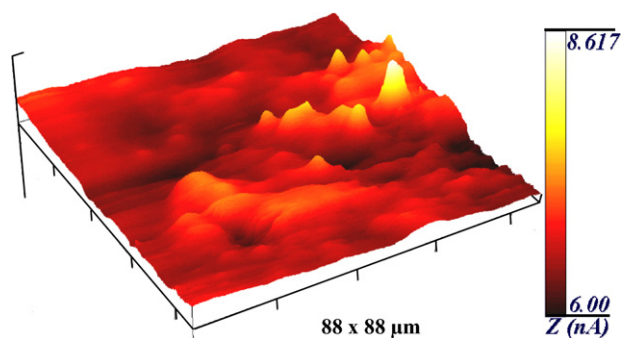


Fig. 11. 3D SECM image of EN AW-3003 alloy surface from integrated AFM/SECM measurement in 20 mM NaCl + 2 mM KI electrolyte during 200 mV anodic polarization. Different currents levels at different active area.

Contrary to the EN AW-3003, it was difficult to obtain clear concurrent AFM/SECM images of the Al–Mn–Si–Zr alloy under the same experimental conditions. It appears that Al–Mn–Si–Zr exhibits a much smaller number of local active areas in the diluted solution, which suggests a higher resistance to initiation of localized corrosion as compared to EN AW-3003. This is in agreement with the Volta potential mapping and the in situ AFM observation.

It should be mentioned that the relationship between the microstructure and pitting precursors seems not so clear from the results obtained by the dual mode AFM/SECM measurements. This is probably due to the fact that the measurements were focused on the initial stage of corrosion process on the well-polished surface, before noticeable changes have occurred in the topography, and as mentioned before, the quality of the AFM images obtained by the dual mode probe was not sufficient to reveal the small changes in topography. It is of great interest to perform the AFM/SECM measurements on the surface area that has been characterized by SEM/EDS and SKPFM. Such effort is being made to clarify the relationship between the microstructure and corrosion initiation sites.

In short, the in situ AFM and integrated AFM/SECM observations indicate that extensive localized dissolution (i.e., active pitting) can occur and develop into wide pitting that expands laterally on the EN AW-3003, whereas the Al–Mn–Si–Zr is more resistant to pitting initiation and the pits are narrow and “tunnel-like”. According to Videm [20], these two types of pitting modes can be found on Al alloys depending if they are formed fast or slowly, observed by polarization of the samples at high or low anodic potentials, respectively. Tunneling predominates at relatively lower potentials whereas conventional (wide) pitting occurs at higher potentials [6]. The pH of the solution and temperature were also observed to influence the pitting mode [1]. In this study, however, fast dissolution and wide pitting occurred on the EN AW-3003 even without anodic polarization, but tunnel-like pitting was dominating on the Al–Mn–Si–Zr in the same solution. Probably the passive film formed on the Al–Mn–Si–Zr is more stable than that on the EN AW-3003. In fact, this was observed by electrochemical impedance measurements in neutral solutions (data not shown).

The influence of individual alloy elements on the corrosion mechanism is a complicated matter for multi-component

Al alloys. The difference in the content of Cu, Si, Mn and Zr between the two alloys investigated may provide some explanation of the observed localized corrosion behavior. It is well known that Cu accentuates the more general mode of corrosion of Al, and this effect seems to be dramatically reduced at 0.04 wt.% Cu. It is generally believed that the great tendency for intergranular corrosion of the EN AW-3003 is due to Cu-rich phases precipitated along grain boundaries, but Sinyavskii et al. claim that this is not the case for an Al alloy with alloying elements well within solubility limits [21]. They instead claim that the cause is the recrystallization process (i.e., crystallographic pitting). The very low Cu content of the Al–Mn–Si–Zr may be the reason for its insensibility to intergranular corrosion. The higher Mn and Si content and lower Fe content of the Al–Mn–Si–Zr alloy results in a higher Mn/Fe ratio in the constituent particles and also in a lower amount of Mn in solid solution. A higher Mn content in the particles (cathodic) is normally beneficial since it lowers the cathodic reduction rate under open-circuit condition. A smaller number of particles having large Volta potential difference relative to the matrix of the Al–Mn–Si–Zr alloy can explain the smaller number of active sites and lower degree of local dissolution on its surface compared to the EN AW-3003. The lower content of Cu and Mn in solid solution of the Al–Mn–Si–Zr leads to a certain decrease in the corrosion potential compared to the EN AW-3003, which may also contribute to a lower degree of susceptibility to pitting corrosion of Al–Mn–Si–Zr. Further studies, especially analysis of the passive film, are necessary to elucidate in more detail the mechanism of local corrosion processes and the influence of individual alloying elements.

4. Conclusion

By utilizing state-of-the-art local probing techniques with micrometer resolution, studies of two 3xxx (Al–Mn) series Al alloys for heat exchange applications, have resulted in a more detailed understanding of the localized corrosion processes of both alloys on a microscopic level. The Volta potential mapping reveals the cathodic character of constituent intermetallic particles relative to Al alloy matrix. The in situ AFM measurements show details of local dissolution and formation of corrosion products around active sites associated with intermetallic particles as well as grain boundaries of the Al alloys. The integrated SECM/AFM imaging of simultaneous topography and electrochemical current provides information of pitting precursors and initiation processes. Concurrent AFM and SECM images of the same surface area have been obtained with micrometer resolution.

The Al–Mn–Si–Zr alloy contains a smaller number of intermetallic particles having larger Volta potential differences relative to the matrix as compared to the EN AW-3003. Some larger micrometer sized intermetallic particles cause localized dissolution initiating at particle–matrix boundary regions, whereas fine dispersoids are not active. On the EN AW-3003 alloy, many active sites and extensive local dissolution result in a higher material loss than on the Al–Mn–Si–Zr alloy. The Al–Mn–Si–Zr alloy contains much less intermetallic particles that initiate localized dissolution and mainly develop into small tunnel-like pits. The result is a lower weight loss, favorable for application as fin material in heat exchange applications.

Acknowledgements

Sapa Heat Transfer AB and the Brinell Centre at the Royal Institute of Technology are acknowledged for their financial support. The authors thank Lars Östensson at Sapa Technology for the SEM–EDS measurements and Namurata Sathirachinda at KIMAB for the assistance in SKPFM measurements.

References

- [1] M. Baumgärtner, H. Kaesche, *Corros. Sci.* 29 (1989) 363.
- [2] M. Baumgärtner, H. Kaesche, *Corros. Sci.* 31 (1990) 231.
- [3] V.S. Sinyavskii, *Prot. Met.* 37 (2001) 469.
- [4] G.S. Frankel, *J. Electrochem. Soc.* 145 (1998) 2186.
- [5] Q. Meng, G.S. Frankel, *J. Electrochem. Soc.* 151 (2004) B271.
- [6] R.C. Newman, *Corros. Sci.* 37 (1995) 527.
- [7] J.O. Park, C.H. Paik, Y.H. Huang, R.C. Alkire, *J. Electrochem. Soc.* 146 (1999) 517.
- [8] M.D. Tkalenko, *Prot. Met.* 37 (2001) 301.
- [9] R.G. Buchheit, R.P. Grant, P.F. Hlava, B. McKenzie, G.L. Zender, *J. Electrochem. Soc.* 144 (1997) 2621.
- [10] T.J.R. Leclerc, R.C. Newman, *J. Electrochem. Soc.* 149 (2002) B52.
- [11] V. Guillaumin, P. Schmutz, G.S. Frankel, *J. Electrochem. Soc.* 148 (2001) B163.
- [12] P. Leblanc, G.S. Frankel, *J. Electrochem. Soc.* 149 (2002) B239.
- [13] J.H.W. de Wit, *Electrochim. Acta* 49 (2004) 2841.
- [14] M. Büchler, J. Kerimo, F. Guillaume, W.H. Smyrl, *J. Electrochem. Soc.* 147 (2000) 3691.
- [15] J.C. Seegmiller, D.A. Buttry, *J. Electrochem. Soc.* 150 (2003) B413.
- [16] A. Davoodi, J. Pan, C. Leygraf, S. Norgren, *Electrochem. Solid-State Lett.* 8 (2005) B21.
- [17] A. Davoodi, J. Pan, C. Leygraf, S. Norgren, *Appl. Surf. Sci.* 252 (2006) 5499.
- [18] M. Jönsson, D. Thierry, N. LeBozec, *Corros. Sci.* 48 (2006) 1193.
- [19] A. Davoodi, J. Pan, C. Leygraf, S. Norgren, *Proceedings on 16th International Corrosion Congress, Beijing, September 19–24, 2005* (paper no.19-19).
- [20] K. Videm, Kjeller Report, KR-149, Norwegian Institute of Atomic Energy, 1974.
- [21] V.S. Sinyavskii, V.V. Ulanova, V.D. Kalinin, *Prot. Met.* 40 (2004) 481.